Enhancing High Harmonic Output in Solids through Quantum Confinement

C. R. McDonald,* K. S. Amin, S. Aalmalki, and T. Brabec
Department of Physics, University of Ottawa, Ottawa, Ontario K1N 6N5, Canada
(Received 27 June 2017; published 3 November 2017)

We investigate theoretically the effect of quantum confinement on high harmonic generation (HHG) in semiconductors by systematically varying the width of a model quantum nanowire. Our analysis reveals a reduction in ionization and a concurrent growth in HHG efficiency with increasing confinement. The drop in ionization results from an increase in the band gap due to stronger confinement. The increase in harmonic efficiency comes as a result of the confinement restricting the spreading of the transverse wave packet. As a result, intense laser driven 1D and 2D nanosystems present a potential pathway to increasing yield and photon energy of HHG in solids.

DOI: 10.1103/PhysRevLett.119.183902

For several decades high harmonic generation (HHG) has provided the foundation for attosecond spectroscopy techniques used to probe the structural and temporal properties of atoms and molecules [1–6]. Recently, HHG has been studied in bulk solids both experimentally [7–14] and theoretically [15–21]. It has been demonstrated that HHG in semiconductor crystals occurs via a three-step process similar to HHG in atomic systems [12,15]. An electron-hole pair is born through ionization, follows a quiver motion in the laser field, and recombines upon recollision whereat it emits a harmonic photon. This provides an avenue through which the tools and techniques of attosecond science developed for atoms and molecules can be applied to solid state systems.

A necessary consideration to use HHG for attosecond applications is the amount of harmonic output and the maximum photon energy that can be produced. While both can be increased by increasing the peak intensity of the driving field, a limit is set by the onset of material damage. Damage is directly linked to the amount of electrons transferred from the valence to the conduction band during HHG.

Analogous to using magnetic fields in atomic gases [22], our theoretical analysis of HHG in model nanowires reveals that quantum confinement transverse to the laser polarization direction holds the potential to mitigate this limitation, thus allowing us to scale up photon energy and harmonic yield. First, transverse confinement of the conduction band wave packet strongly reduces ionization. Therefore, the damage threshold is expected to increase. Second, the harmonic yield per ionization event increases with decreasing wire width; i.e., reduced ionization is countered by more efficient HHG. Considerable enhancement of harmonic yield per ionization event compared to bulk HHG is found for wire widths starting around 10–30 nm depending on the laser wavelength. Enhancement increases towards longer wavelengths and exponentially with decreasing wire extent.

This behavior is traced back to two physical mechanisms. (i) The material band gap increases with decreasing wire width resulting in reduced ionization. (ii) Quantum confinement results in a reduction of the available transverse states reducing quantum diffusion and therefore wave packet spreading during the quiver motion of the electron-hole pair. Accordingly, the recollision cross section and therefore harmonic yield is increased. Our findings offer a potential explanation for the increase in harmonic efficiency found in recent experiments, where bulk HHG was compared to atomically thin monolayers of crystalline MoS_2 [23]. The theoretical findings reported here suggest that HHG in a forest of quantum wires, in atomically thin 2D layers, or in an array of ultrathin wires on a substrate present a potential pathway towards scaling HHG to higher efficiencies and photon energies.

The single-active-electron approximation was found to give a reasonable description of strong field processes in bulk solids [15–21,24]. Our work focuses on developing a simple picture for identifying and understanding the single-electron aspects of transverse quantum confinement on strong field processes in solids. In the conclusion we will discuss how the inclusion of correlation effects might alter our results. All equations are presented in atomic units, however, all parameters will be provided in SI units. Our model nanowire consists of a single conduction and a single valence band. Each three-dimensional band is the sum of three one-dimensional bands. In the longitudinal direction z along laser polarization a direct band gap with typical semiconductor parameters is used. The band gap along each transverse direction is determined by a periodic potential $v(u)$ $(u = x, y)$. For a single lattice site of width a_u and well of depth v_0 this is given by

$$v(u) = \begin{cases} v_0 e^{-\frac{u^2}{\sigma_u^2 - u^2}} & \text{for } 0 \le u < \sigma_u \\ v_0 e^{-\frac{(u-a_u)^2}{\sigma_u^2 - (u-a_u)^2}} & \text{for } a_u - \sigma_u < u \le a_u \\ 0 & \text{otherwise,} \end{cases} \quad (1)$$

where $\sigma_u = 0.41$ Å. The width of the nanowire L_u is determined by selecting the number of lattice sites. The resulting 1D Hamiltonians are diagonalized numerically. For simplicity, both transverse directions have identical confinements; we denote the width of the nanowire as $L = L_{x,y}$.

Transverse confinement causes the band structure to form a discrete set of states. We express the band gap for the nanowire as $\varepsilon_L(\mathbf{k}) = \bar{\varepsilon}_L(\mathbf{n}_\perp) + \varepsilon_\parallel(k_\parallel)$, where $\bar{\varepsilon}_L(\mathbf{n}_\perp) = E_g + \varepsilon_\perp(\mathbf{n}_\perp, L)$ and $\varepsilon_\perp$ and $\varepsilon_\parallel$ are band gaps in the transverse and longitudinal directions to the field; E_g is the minimum band gap of the bulk crystal. Here we define $\mathbf{k} = (\mathbf{n}_\perp, k_\parallel)$ with $\mathbf{n}_\perp = (n_x, n_y)$ being the quantum numbers of the transverse states and $k_\parallel = k_z$ being the longitudinal crystal momentum. The minimum band gap energy of the nanowire is denoted by $E_L = \bar{\varepsilon}_L(1,1)$, with $n_x = n_y = 1$ being the lowest transverse level. Further, we denote the bandwidth of our nanowire as $\Delta_L = \max[\varepsilon_L(\mathbf{k})]$. Finally, when discussing the bulk material along the transverse direction, we will drop the L label and replace $\mathbf{n}_\perp$ with $\mathbf{k}_\perp = (k_x, k_y)$, the usual crystal momentum.

Our calculations use $E_g = 3.3$ eV as the minimum band gap in the bulk crystal. The longitudinal band gap $\varepsilon_\parallel$ is unaffected by the confinement and is given by a Fourier cosine expansion. The Fourier coefficients and transition dipole are given in Ref. [[16]]; the band gap along k_z is shown in Fig. 1(a). The lattice periodicity and effective mass are $a_z = 2.8$ Å and $m_z = 0.098 m_e$.

The wells have a depth of $v_0 = 13.6$ eV and a lattice spacing of $a = a_{x,y} = 5$ Å. In the bulk limit the effective transverse mass is $m_{x,y} = 0.053 m_e$; Fig. 1(b) shows the transverse band gap in this limit. As a result of the quantum confinement, the transverse band structure is arranged into discrete levels; this is demonstrated for $L = 2$ nm in Fig. 1(c). Further, confinement increases the band gap as the wire becomes narrower; see Fig. 1(d). Our calculations consider wires in the range from $L = 50$ nm, where the band structure is approximately that of the bulk, down to $L = 1$ nm, where there are only two atomic sites along each transverse direction.

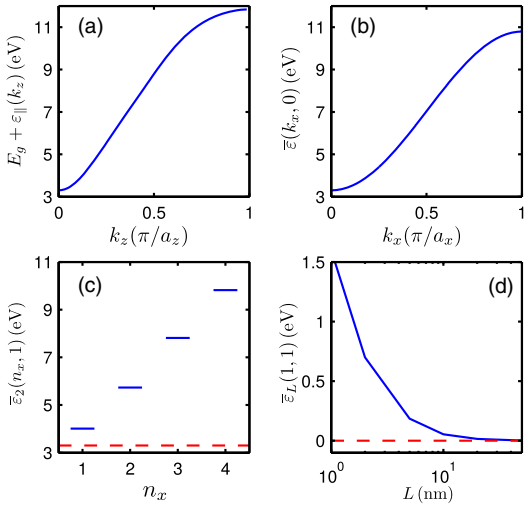

FIG. 1. (a) Band gap along the longitudinal and (b) transverse x direction for the bulk crystal. (c) Band gap along the transverse x direction for a nanowire with $L = 2$ nm. (d) Increase in band gap energy resulting from confinement along a single transverse axis; the dashed lines in (c) and (d) represent the bulk limit.

Our analysis utilizes the frozen valence band approximation [24], where it is assumed that the population in the valance band remains unchanged during the pulse. Under this assumption, the population transferred to the conduction band is given by

$$n_c(t) = \mathcal{N} \int_{\bar{\mathrm{BZ}}} d^3K \left| \int_{-\infty}^{t} dt' \Omega^*(\mathbf{K}, t') e^{iS(\mathbf{K},t')} \right|^2, \quad (2)$$

where $S(\mathbf{K}, t) = \int_{-\infty}^{t} \varepsilon_L(\mathbf{K} + \mathbf{A}(t'))dt'$ with $\mathbf{A}(t)$ being the vector potential. The crystal momentum $\mathbf{k} = \mathbf{K} + \mathbf{A}(t)$ and Brillouin zone $\bar{\mathrm{BZ}} = \mathrm{BZ} - \mathbf{A}(t)$ have been transformed into a frame moving with $\mathbf{A}(t)$; $\mathcal{N}$ is a constant that ensures normalization of the initial valence band population. Further, $\Omega(\mathbf{K}, t) = \mathbf{d}(\mathbf{K} + \mathbf{A}(t)) \cdot \mathbf{F}(t)$ with $\mathbf{d}$ the dipole transition moment; the electric field is determined through $\mathbf{F}(t) = -d\mathbf{A}/dt$. In our calculations below, we will be interested in the final conduction band population versus L, which we denote $n_c(L) = n_c(L, t = \infty)$. The L dependence enters through the band structure ε_L in $S(\mathbf{K}, t)$. The wave function is normalized to unity for each L to ensure an equivalent amount of material is considered when comparing different L's. This means that four nanowires with width $L/2$ are compared with a single nanowire of width L.

High harmonic generation in solids results from two sources—an interband and an intraband current [25]. The interband term, as calculated in length gauge [26], was demonstrated to be the dominant contributor to above band gap harmonics for semiconductors exposed to mid-IR fields [12,15]. As such, in this work we will focus on the interband term; we have verified that the intraband term is negligible, in the above band gap range, for all cases considered here. However, we note that in the presence of strong dephasing or THz fields the intraband harmonics may become a significant contributor to HHG [9,15]. In the frozen valence band approximation, the interband current can be written as [15],

$$\mathbf{j}(\omega) = \mathcal{N}\omega \int_{\bar{\mathrm{BZ}}} d^3\mathbf{K} \int_{-\infty}^{\infty} dt e^{-i\omega t} \mathbf{d}^*(\mathbf{K} + \mathbf{A}(t)) e^{-iS(\mathbf{K},t)} \times \int_{-\infty}^{t} dt' \Omega(\mathbf{K}, t') e^{-iS(\mathbf{K},t')} + \mathrm{c.c.} \quad (3)$$

The harmonic spectrum is determined by taking the magnitude square of Eq. (3). As a measure of the harmonic efficiency we define the harmonic yield Φ as,

$$\Phi(L) = \int_{E_L}^{E_L+\Delta_L} d\omega |\mathbf{j}(\omega)|^2. \quad (4)$$

Hence, $\Phi(L)$ is the total contribution of the allowed above band gap harmonics; see the inset of Fig. 2(d). Finally, we define the yield ratio as $\Phi(L)/n_c(L)$. This gives a measure of the harmonic yield per ionization event.

Our model solid is exposed to an intense laser-field with vector potential $\mathbf{A}(t) = \hat{z}(F_0/\omega_0)f(t)\cos(\omega_0 t)$, where $F_0 = 0.26$ V · Å^{-1} is the peak field strength ($I_0 = 8.8 \times 10^{11}$ W · cm^{-2}) and ω_0, λ_0 are the laser driver frequency and wavelength; the pulse envelope $f(t)$ is Gaussian with a FWHM of three cycles. Figure 2(a) shows the time-dependent conduction band population for $L = 50$ nm (blue) and $L = 1$ nm (red) for $\lambda_0 = 6.4$ μm. The final conduction band population versus L is presented in Fig. 2(b) for $\lambda_0 = 3.2$ μm (solid) and $\lambda_0 = 6.4$ μm (dash-dot). When $L = 50$ nm ionization has plateaued and is close to that of the bulk crystal. As L is decreased to 1 nm, the final conduction band population drops by several orders of magnitude. This behavior can be attributed to the increase in the band gap caused by quantum confinement. For few-cycle pulses used here optical field ionization is the dominant mechanism resulting in material damage; other ionization channels, such as collisional ionization, are of subordinate importance. Damage occurs once the conduction band population reaches the percent level. As a result, from Fig. 2(b) it follows that the damage threshold intensity increases with decreasing L.

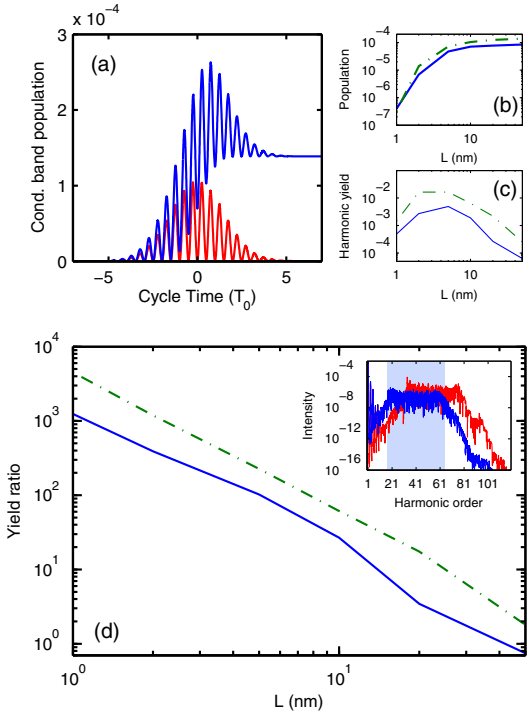

FIG. 2. (a) Conduction band population dynamics for $L = 50$ (blue) and $L = 1$ nm (red) with $\lambda_0 = 6.4$ μm. (b) Final conduction band population, (c) harmonic yield, and (d) yield ratio versus L for $\lambda_0 = 3.2$ (solid) and $\lambda_0 = 6.4$ μm (dash-dot). The inset shows harmonic spectra for $L = 50$ (blue) and $L = 1$ nm (red). The shaded region shows the above band gap range $[E_L, E_L + \Delta_L]$ for the 50 nm wire. The spectrum for the 1 nm wire is shifted due to the increase in band gap and thus the region of integration is shifted accordingly.

Further, the time dynamics of the conduction band population for the 50 nm wire shows synchronous growth with the laser half-cycle, in agreement with semiconductor experiments [27]. By contrast, the 1 nm wire displays mainly transient population dynamics with a small carrier density remaining after the pulse, similar to that observed in dielectric experiments [28]. This opens the possibility to nanoengineer semiconductor materials to be used in PHz optoelectronics where so far the primary candidates are dielectrics [29,30] or graphene [31].

Figure 2(c) shows the harmonic yield calculated from Eq. (4). Here we see that from $L = 50$ to $L = 1$ nm there is approximately an order of magnitude increase in the harmonic output. For $L < 3$–4 nm the increase in HHG is outweighed by the drop in ionization so that HHG efficiency declines with decreasing L. The harmonic yield is higher for the longer wavelength mainly due to higher ionization. For the parameters used here, the wavelength dependence of the HHG process, after ionization, has already saturated at 3.2 μm [see Fig. 3(b)].

Figures 2(a)–2(c) display an increase in harmonic yield accompanied by a significant decrease in ionization.

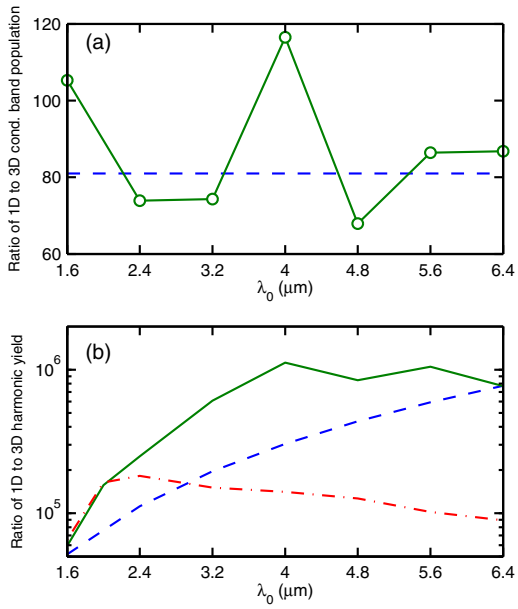

FIG. 3. (a) Ratio of final conduction band population in the 1D system to the $L = 50$ nm nanowire (circles with solid line) versus λ_0; the dashed line gives $n_c^{\perp -1}$ predicted by Eq. (5). (b) Ratio of harmonic output from the 1D system to the $L = 50$ nanowire (solid) and the $L = 20$ nm nanowire (dash-dot) versus λ_0. The dashed line shows the prediction for $|j_\perp|^{-2}$ from Eq. (6).

As such, it is helpful to consider the yield ratio—harmonic yield per ionization event—shown in Fig. 2(d). This constitutes a measure of how efficiently population promoted to the conduction band generates above band gap harmonic radiation. Figure 2(d) displays a monotonic growth in yield ratio with decreasing wire width implying that the efficiency with which electrons promoted to the conduction band create harmonics is greatly increased. Comparing the $L = 50$ nm to $L = 1$ nm, there is an increase of nearly 3 orders of magnitude. As ionization is the first step in HHG, an increase in harmonic yield efficiency coupled with a decrease in ionization appears counterintuitive; in what follows we will explain this surprising result.

Quantum confinement results in an increase of the band gap and in a reduction of the density of transverse states. Both effects influence ionization and HHG. By varying L, as is done in Fig. 2, these contributions remain coupled. To quantify these contributions, they must be separated. This is achieved by noting that the ultimate limit of confinement is represented by a chain of atoms with only one atom along the transverse directions. The single atom wire has only one doubly degenerate transverse state and therefore is identical to an idealized 1D system with the same band gap in which transverse coordinates are neglected. We have verified in our calculations that this limit is reached for $L = 1$ nm, a wire with two atomic sites in each transverse direction. Similarly, by neglecting the transverse coordinates of a 3D bulk material, the band gap of the resulting 1D medium remains unchanged; however, quantum confinement is changed from zero to maximum. Thus, comparison of a 3D bulk medium to its corresponding 1D limit explores the effects of quantum confinement only. Comparison of the 1D limit to the $L = 1$ nm wire quantifies the effect coming from the change of the band gap.

Additional insight can be obtained by an analytical comparison of 3D bulk to its 1D limit. This is done for ionization and HHG, as both can be represented as a product of transverse and longitudinal terms. We begin with the analytical comparison and then compare it to numerical results. Following the Keldysh-Lewenstein approach [32,33], we apply saddle point integration to Eq. (2) followed by integration over $k_{x,y}$ (see Supplemental Material [34]). The conduction band population $n_c = n_c^{1D} n_c^{\perp}$ can then be split into longitudinal n_c^{1D} and transverse $n_c^{\perp}$ contributions where,

$$n_c^{\perp} = \frac{a_x a_y}{2\pi} \sqrt{\frac{m_x m_y F_0^2}{2 m_z E_g}}. \tag{5}$$

Similarly, in Eq. (3), the 3D current j_{3D} can also be split into longitudinal j_{1D} and transverse $j_{\perp}$ contributions [34], where

$$|j_{\perp}|^2 = a_x a_y m_x m_y \left(\frac{2 m_z E_g}{F_0^2} + \frac{\pi^2}{\omega_0^2} \right)^{-1}. \tag{6}$$

Note that Eqs. (5) and (6) scale differently with $m_{x,y}$. Consequently, changing the effective mass of the electron-hole pairs by using different materials will have a stronger influence on HHG than on ionization. Finally, for the above expression to be valid, the Keldysh parameter must satisfy $\gamma < 1$; all calculations presented here have $0.22 < \gamma < 0.87$ [34].

To test Eqs. (5) and (6) we compare the $L = 50$ nm wire to its corresponding 1D system where the transverse coordinates have been neglected. Figure 3(a) shows the ratio of the final conduction band population from Eq. (2) of the 1D system to the $L = 50$ nm wire as compared to $n_c^{\perp -1}$ from Eq. (5) (dashed line). Equation (5) is wavelength independent and the calculated results appear consistent with this. While the calculated results deviate from a constant value, given the simplicity of Eq. (5) and the complex nature of ionization in solids [24], these variations are completely reasonable. Further, the results in Fig. 3(a) indicate that ionization is not strongly affected by the form of the wave packet at birth. Thus, the drop in ionization seen in Fig. 1(b) results mainly from the band gap increase.

Figure 3(b) shows the ratio of harmonic output from Eq. (3) of the 1D system to the $L = 50$ nm (solid) and the $L = 20$ nm (dash-dot) wires; these are compared to $|j_{\perp}|^{-2}$ predicted by Eq. (6) (dashed line). The result in Eq. (6) predicts that the ratio of 1D to 3D harmonic output will increase with wavelength. This rise results from reduced harmonic output of the 3D system due to quantum diffusion which decreases the electron-hole recombination cross section. For the 50 nm wire this ratio increases until about 4 μm and then begins to saturate, indicating a halt in spreading of the wave packet due to the confinement. Similar behavior occurs for the $L = 20$ nm wire but saturation begins at a shorter wavelength. This is consistent with that expected from quantum diffusion. Longer wavelengths experience greater spreading of the transverse wave packet and will thus be affected more strongly by a narrower confinement. Finally, our analytical model reflects the trend correctly, but the λ_0^2 scaling in Eq. (6) understates the power scaling of the wavelength dependence. This indicates that the actual ionized transverse wave packet structure might be more complex than the approximate Gaussian distribution obtained in Eqs. (5) and (6). Such a fact might also explain the unusual elliptic polarization dependence of HHG in solids observed by experiment [35].

We have demonstrated theoretically that quantum confinement provides a systematic way to increase the harmonic efficiency of a material. A simple picture of the main physical mechanisms has been developed at the neglect of correlation effects. For low dimensional, tightly confined systems, correlation effects can become strong. This will

restrict the amount by which the minimum band gap is increased as the confinement width is lowered. Further, in confined systems, electrons and holes experience stronger Coulomb interaction [36,37] leading to an increased recollision probability and, by extension, further enhancement of HHG [23].

Finally, our investigation is microscopic in nature—propagation effects have been neglected. A primary limitation to bulk HHG comes from reabsorption of the generated harmonic radiation. Using nanowires can potentially mitigate this limitation, as the effective density of nanowire arrays is considerably lower than the bulk density. Because of the resulting longer interaction lengths phase mismatch between fundamental and harmonic beam might become relevant.

*cmcdo059@uottawa.ca

[1] P. B. Corkum, Plasma Perspective on Strong Field Multiphoton Ionization, Phys. Rev. Lett. **71**, 1994 (1993).

[2] P. B. Corkum and F. Krausz, Attosecond science, Nat. Phys. **3**, 381 (2007).

[3] J. Itatani, J. Levesque, D. Zeidler, H. Niikura, H. Pépin, J. C. Kieffer, P. B. Corkum, and D. M. Villeneuve, Tomographic imaging of molecular orbitals, Nature (London) **432**, 867 (2004).

[4] S. Baker, J. S. Robinson, C. A. Haworth, H. Teng, R. A. Smith, C. C. Chirila, M. Lein, J. W. G. Tisch, and J. P. Marangos, Probing proton dynamics in molecules on an attosecond time scale, Science **312**, 424 (2006).

[5] H. J. Wörner, J. B. Bertrand, D. V. Kartashov, P. B. Corkum, and D. M. Villeneuve, Following a chemical reaction using high-harmonic interferometry, Nature (London) **466**, 604 (2010).

[6] H. J. Wörner *et al.*, Conical intersection dynamics in NO_2 probed by homodyne high-harmonic spectroscopy, Science **334**, 208 (2011).

[7] S. Ghimire, A. D. DiChiara, E. Sistrunk, P. Agostini, L. F. DiMauro, and D. A. Reis, Observation of high-order harmonic generation in a bulk crystal, Nat. Phys. **7**, 138 (2011).

[8] B. Zaks, R. B. Liu, and M. S. Sherwin, Experimental observation of electron-hole recollisions, Nature (London) **483**, 580 (2012).

[9] O. Schubert *et al.* Sub-cycle control of terahertz high-harmonic generation by dynamical Bloch oscillations, Nat. Photonics **8**, 119 (2014).

[10] M. Hohenleutner, F. Langer, O. Schubert, M. Knorr, U. Huttner, S. W. Koch, M. Kira, and R. Huber, Real time observation of interfering crystal electrons in high-harmonic generation, Nature (London) **523**, 572 (2015).

[11] T. T. Luu, M. Garg, S. Yu. Kruchinin, A. Moulet, M. Th. Hassan, and E. Goulielmakis, Extreme ultraviolet high-harmonic spectroscopy of solids, Nature (London) **521**, 498 (2015).

[12] G. Vampa, T. J. Hammond, N. Thiré, B. E. Schmidt, F. Légaré, C. R. McDonald, T. Brabec, and P. B. Corkum, Linking high harmonic generation from gases and solids, Nature (London) **522**, 462 (2015).

[13] G. Vampa, T. J. Hammond, N. Thiré, B. E. Schmidt, F. Légaré, C. R. McDonald, T. Brabec, D. D. Klug, and P. B. Corkum, All-Optical Reconstruction of Crystal Band Structure, Phys. Rev. Lett. **115**, 193603 (2015).

[14] G. Ndabashimiye, S. Ghimire, M. Wu, D. A. Browne, K. J. Schafer, M. B. Gaarde, and D. A. Reis Solid-state harmonics beyond the atomic limit, Nature (London) **534**, 520 (2016).

[15] G. Vampa, C. R. McDonald, G. Orlando, D. D. Klug, P. B. Corkum, and T. Brabec, Theoretical Analysis of High Harmonic Generation in Solids, Phys. Rev. Lett. **113**, 073901 (2014).

[16] G. Vampa, C. R. McDonald, G. Orlando, P. B. Corkum, and T. Brabec, Semiclassical analysis of high harmonic generation in bulk crystals, Phys. Rev. B **91**, 064302 (2015).

[17] P. G. Hawkins and M. Yu. Ivanov, Role of subcycle transition dynamics in high-order-harmonic generation in periodic structures, Phys. Rev. A **87**, 063842 (2013).

[18] A. F. Kemper, B. Moritz, J. K. Freericks, and T. P. Devereaux, Theoretical description of high-order harmonic generation in solids, New J. Phys. **15**, 023003 (2013).

[19] M. Wu, S. Ghimire, D. A. Reis, K. J. Schafer, and M. B. Gaarde, High-harmonic generation from Bloch electrons in solids, Phys. Rev. A **91**, 043839 (2015).

[20] C. R. McDonald, G. Vampa, P. B. Corkum, and T. Brabec, Interband Bloch oscillation mechanism for high harmonic generation in semiconductor crystals, Phys. Rev. A **92**, 033845 (2015).

[21] E. N. Osika, A. Chacon, L. Ortmann, N. Suarez, J. A. Perez-Hernandez, B. Szafran, M. F. Ciappina, F. Sols, A. S. Landsman, and M. Lewenstein, Wannier-Bloch Approach to Localization in High-Harmonics Generation in Solids, Phys. Rev. X **7**, 021017 (2017).

[22] D. B. Milošević and A. F. Starace, Magnetic-Field-Induced Intensity Revivals in Harmonic Generation, Phys. Rev. Lett. **82**, 2653 (1999).

[23] H. Liu, Y. Li, Y. S. You, S. Ghimire, T. F. Heinz, and D. A. Reis, High harmonic generation from an atomically thin semiconductor, Nat. Phys. **13**, 262 (2017).

[24] C. R. McDonald, G. Vampa, P. B. Corkum, and T. Brabec, Intense-Laser Solid State Physics: Unraveling the Difference Between Semiconductors and Dielectrics, Phys. Rev. Lett. **118**, 173601 (2017).

[25] D. Golde, T. Meier, and S. W. Koch, High harmonics generated in semiconductor nanostructures by the coupled dynamics of optical inter- and intraband excitations, Phys. Rev. B **77**, 075330 (2008).

[26] P. Földi, Gauge invariance and interpretation of interband and intraband processes in high-order harmonic generation from bulk solids, Phys. Rev. B **96**, 035112 (2017).

[27] M. Schultze *et al.*, Attosecond bandgap dynamics in silicon, Science **346**, 1348 (2014).

[28] M. Schultze *et al.*, Controlling dielectrics with the electric field of light, Nature (London) **493**, 75 (2013).

[29] A. Schiffrin *et al.*, Optical-field-induced current in dielectrics, Nature (London) **493**, 70 (2013).

[30] A. Sommer *et al.*, Attosecond nonlinear polarization and light-matter energy transfer in solids, Nature (London) **534**, 86 (2016).

[31] T. Higuchi, Ch. Heide, K. Ullmann, H. B. Weber, and P. Hommelhoff, Light-field driven currents in graphene, arXiv:1607.04198v1.

[32] L. Keldysh, Ionization in the field of a strong electromagnetic wave, Sov. Phys. JETP **20**, 1307 (1965).

[33] M. Lewenstein, P. Balcou, M. Y. Ivanov, A. L'Huillier, and P. B. Corkum, Theory of high harmonic generation by low-frequency laser fields, Phys. Rev. A **49**, 2117 (1994).

[34] See Supplemental Material at http://link.aps.org/supplemental/10.1103/PhysRevLett.119.183902 for a derivation of Eqs. (5) and (6).

[35] Y. S. You, D. A. Reis, and S. Ghimire, Anisotropic high-harmonic generation in bulk crystals, Nat. Phys. **13**, 345 (2017).

[36] K. He, N. Kumar, L. Zhao, Z. Wang, K. F. Mak, H. Zhao, and J. Shan, Tightly Bound Excitons in Monolayer WSe_2, Phys. Rev. Lett. **113**, 026803 (2014).

[37] A. Chernikov, T. C. Berkelbach, H. M. Hill, A. Rigosi, Y. Li, O. B. Aslan, D. R. Reichman, M. S. Hybertsen, and T. F. Heinz, Exciton Binding Energy and Nonhydrogenic Rydberg Series in Monolayer WS_2, Phys. Rev. Lett. **113**, 076802 (2014).